JGR: Solid Earth

Supporting Information for

The interplay of rifting, magmatism and formation of geothermal resources in the Ethiopian Rift constrained by 3-D magnetotelluric imaging

DOI:

M.L.T. Dambly[1], F. Samrock[1], A.V. Grayver[2,3], and M.O. Saar[1,4]

[1] Geothermal Energy and Geofluids group, Institute of Geophysics, ETH Zurich, Switzerland
[2] Institute of Geophysics and Meteorology, University of Cologne, Germany
[3] Earth and Planetary Magnetism group, Institute of Geophysics, ETH Zurich, Switzerland
[4] Department of Earth and Environmental Sciences, University of Minnesota, USA

Corresponding author: M.L.T. Dambly, Institute of Geophysics, ETH Zurich, Sonneggstrasse 5, 8092 Zurich, Switzerland (mdambly@ethz.ch)

Contents of this file

Introduction The supplementary information includes basic equations explaining the MT method (Text S1.); information on the MT dataset and how apparent resistivities of the starting model were obtained from SSQ-impedances (Text S2.); details on the mesh used for inversion and forward modelling (Text S3.); a comparison of the best fitting phase tensor and impedance tensor models (Text S4.1); an in-depth analysis of the data fit for the final impedance and phase tensor model (Text S4.2. and S4.3.); details about the melt fraction estimation in the lower crustal magma ponding zone (Text S5.1.); details about electrical conductivities in the shallow aquifer/sediment unit (C1) (Text S5.2.); and results of tests investigating the sensitivity of the model to a high conductivity anomaly in the western study area (Text S6.); a map of the Moho-depth (Fig. S17); and a figure showing the final model alongside with shallow seismicity in the area (Fig. S18).

Text S1. In the magnetotelluric (MT) method, the natural variations of the electric and magnetic field are measured on the Earth's surface. In the frequency domain, the magnetic field ($\mathbf{H}$) can be linearly related to the electric field ($\mathbf{E}$) through a transfer function, known as impedance tensor ($\mathbf{Z}$):

$$\begin{pmatrix} E_x(\mathbf{r},\omega) \\ E_y(\mathbf{r},\omega) \end{pmatrix} = \begin{pmatrix} Z_{xx}(\mathbf{r},\omega) & Z_{xy}(\mathbf{r},\omega) \\ Z_{yx}(\mathbf{r},\omega) & Z_{yy}(\mathbf{r},\omega) \end{pmatrix} \begin{pmatrix} H_x(\mathbf{r},\omega) \\ H_y(\mathbf{r},\omega) \end{pmatrix}. \tag{1}$$

Here E_i and H_i ($i \in [x, y]$) are the North (X) and East (Y) components of electric and magnetic field variations. $\mathbf{Z}$ depends on the angular frequency $\omega = 2\pi f$ and the position vector ($\mathbf{r}$). Although omitted from equation above, but all quantities also depend on distribution of the subsurface electrical conductivity $\sigma(\mathbf{r})$. Note that the reciprocal of electrical conductivity, resistivity ($\rho = 1/\sigma$), is often used interchangeably.

The complex-valued tensor elements Z_{ij} are commonly plotted in terms of their phase

$$\phi_{ij} = \tan^{-1}\left(\frac{\mathrm{Im}(Z_{ij})}{\mathrm{Re}(Z_{ij})}\right), \quad i, j \in [x, y]. \tag{2}$$

and apparent resistivity

$$\rho_{a,ij} = \frac{|Z_{ij}|^2}{\omega\mu_0}, \quad i, j \in [x, y], \tag{3}$$

where μ_0 is the magnetic permeability of free space $\mu_0 = 4\pi * 10^{-7}\,\mathrm{Vs/Am}$.

Information about the dimensionality and directionality of the conductivity structures can be obtained from the phase tensor ($\mathbf{\Phi}$) (e.g. *Caldwell et al.*, 2004):

$$\mathbf{Z} = \mathrm{Re}(\mathbf{Z}) + \mathrm{Im}(\mathbf{Z}) = X + iY, \quad \mathbf{\Phi} = X^{-1}Y \tag{4}$$

The phase tensor $\mathbf{\Phi}$ can be visualized as an ellipse, that is mathematically described by one direction (α) and three rotational invariants ($\beta, \Phi_{min}, \Phi_{max}$), where $\mathbf{R}$ is the rotation matrix:

$$\mathbf{\Phi} = \mathbf{R}^T(\alpha - \beta) \begin{pmatrix} \Phi_{max} & 0 \\ 0 & \Phi_{min} \end{pmatrix} \mathbf{R}(\alpha + \beta) \tag{5}$$

The tilt angle ($\alpha - \beta$) of the $\mathbf{\Phi}$-ellipse represents the electric strike direction at the measurement location for the respective sounding period. In case of a 2-D subsurface Φ_{min} and Φ_{max} will be parallel and perpendicular to the linearly polarized $\mathbf{E}$- and $\mathbf{H}$-fields.

Text S2. The magnetotelluric dataset of our study is a combination of different surveys conducted by ETH Zurich, the Geological Survey of Ethiopia (GSE) and the RiftVolc project, as summarized in Table S1.

Dataset	Measured by	Study	Survey Area	Average MT site spacing		Number of MT sites	Inversion
Local at Aluto	ETH Zurich & GSE	*Samrock et al.* (2015) *Cherkose and Mizunaga* (2018) *Samrock et al.* (2020)	Grid:5 x 15 km	0.7 km		165	ModEM 3-D: $\mathbf{Z}$ ModEM 3-D: $\mathbf{Z}$ GoFEM 3-D: $\mathbf{\Phi}$
Regional across rift	RiftVolc Project	*Hübert et al.* (2018)	Profile: 120 km	4.3 km	5.9 km	25	EMILIA 2D: DET mode
Regional western rift		-	Profile: 32 km	9.6 km		4	-
		-	Profile: 51 km	12.9 km		4	-

Table S1: Information on the MT datasets analyzed in this study. MT data from the surveys of the RiftVolc project are publicly available for download (*Hübert and Whaler*, 2020) as well as ETH survey data (*Samrock et al.*, 2010). Detailed information about the different inversion codes can be found in (*Kelbert et al.*, 2014) (ModEM 3-D) and in (*Kalscheuer et al.*, 2008) (EMILIA 2D).

Text S2.1. Following (*Rung-Arunwan et al.*, 2016), we calculated SSQ-responses over N_s stations to obtain Z^{1D}_{SSQ} (Eq. 7). Further averaging Z^{1D}_{SSQ} over all periods gives a homogeneous model ($\bar{Z}^{1D}_{SSQ}$: Eq. 8). Starting models based on a regional 1-D SSQ-average have been proved to enable successful phase tensor inversion (e.g. *Rung-Arunwan et al.*, 2022).

$$Z_{SSQ}(\mathbf{r},\omega) = \sqrt{(Z_{xx}(\mathbf{r},\omega)^2 + Z_{xy}(\mathbf{r},\omega)^2 + Z_{yx}(\mathbf{r},\omega)^2 + Z_{yy}(\mathbf{r},\omega)^2)/2} \tag{6}$$

$$Z^{1D}_{SSQ}(\omega) = \sqrt[N_s]{\prod_{i=1}^{N_s} Z_{SSQ}(\mathbf{r}_i,\omega)} \tag{7}$$

$$\bar{Z}^{1D}_{SSQ} = \sqrt[N_p]{\prod_{i=1}^{N_p} Z^{1D}_{SSQ}(\omega_i)} \tag{8}$$

$$\rho_{a,SSQ}(\omega) = \frac{|Z_{SSQ}(\omega)|^2}{\omega\mu_0}, \quad \phi_{SSQ}(\omega) = \tan^{-1}\left(\frac{\mathrm{Im}(Z_{SSQ}(\omega))}{\mathrm{Re}(Z_{SSQ}(\omega))}\right) \tag{9}$$

$$\rho^{1D}_{a,SSQ}(\omega) = \frac{|Z^{1D}_{SSQ}(\omega)|^2}{\omega\mu_0}, \quad \phi^{1D}_{SSQ}(\omega) = \tan^{-1}\left(\frac{\mathrm{Im}(Z^{1D}_{SSQ}(\omega))}{\mathrm{Re}(Z^{1D}_{SSQ}(\omega))}\right) \tag{10}$$

$$\bar{\rho}^{1D}_{a,SSQ} = \sqrt[N_T]{\prod_{i=1}^{N_T} \rho^{1D}_{a,SSQ}(\omega_i)}, \quad \bar{\phi}^{1D}_{SSQ} = \sqrt[N_T]{\prod_{i=1}^{N_T} \phi^{1D}_{SSQ}(\omega_i)} \tag{11}$$

The apparent resistivities $\rho_{a,SSQ}$ and phases ϕ_{SSQ} obtained from Z_{SSQ} at each MT site (Eq. 9) and the corresponding regional averages over all sites ($\rho^{1D}_{a,SSQ}, \phi^{1D}_{SSQ}$ from Eq. 10) are shown in Fig. S1.

Text S2.2. Information about the penetration depth z_p of the MT signal comes from the real part of the C-response $\mathrm{Re}(C)$, that we derived from the regional average impedance (Z^{1D}_{SSQ}, Eq. 7). The C-response is a transfer function related to the 1-D impedance by $Z^{1D} = -i\omega\mu_0 C$ and has units of metres. Following *Weidelt* (1972) and *Schmucker and Weidelt* (1975), $2 * \mathrm{Re}(C)$ represents a proxy for the penetration depth at a given period.

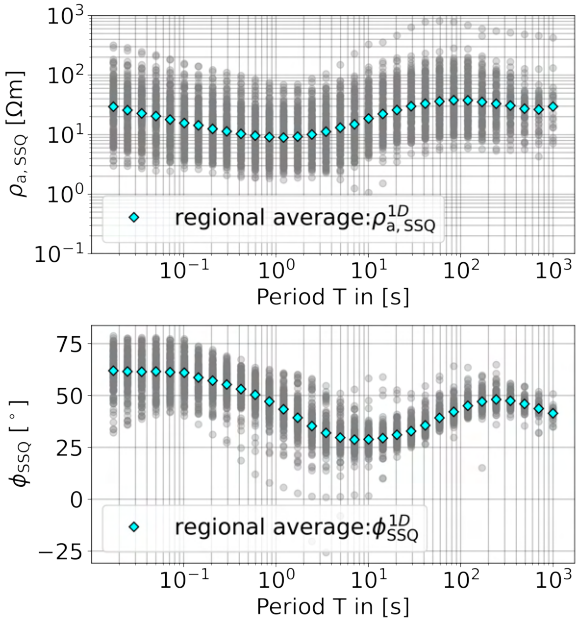

Figure S1: Apparent resistivity ($\rho_{a,SSQ}$) and phases (ϕ_{SSQ}) curves for all stations (gray) and the regional mean values (i.e., $\rho^{1D}_{a,SSQ}$ and $\phi^{1D}_{a,SSQ}$) (blue diamonds).

$$z_p = 2 * \mathrm{Re}\left(\frac{-\bar{Z}^{1D}_{SSQ}}{i\omega\mu_0}\right), \tag{12}$$

Additional information about the penetration depth comes from the skin depth z_s, defined as

$$z_s = \sqrt{\frac{2\bar{\rho}^{1D}_{a,SSQ}}{\mu_0\omega}}. \tag{13}$$

For the periods in our dataset and for the regional mean resistivity, the penetration depth z_p is estimated to be 0.49 km for the shortest and 92.5 km for the longest sounding period (Fig. S2). For the denser station spacing at Aluto ($d_{st} = 0.7\,\mathrm{km}$), the sounding volume overlaps between neighboring sites is given at all periods, whereas outside Aluto area where site spacing is larger ($d_{st} \approx 5.9\,\mathrm{km}$), overlapping sounding volume is given at periods longer than 4.97 s.

Text S2.3. The dominating geoelectric strike over all periods of the entire dataset of this study is aligned with north (Fig. S3), hence we did not rotate the data prior to the inversion.

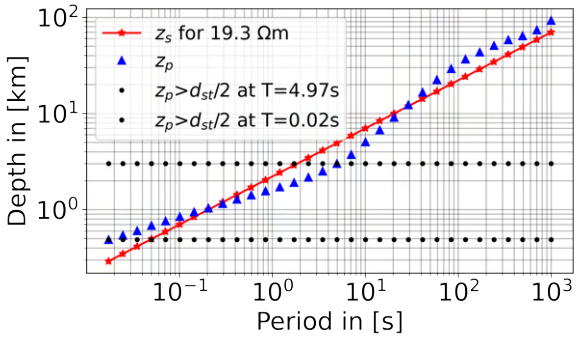

Figure S2: Period-dependent penetration depth z_p (Eq. 12) obtained from Z^{1D}_{SSQ} (Eq. 7) together with the skin depth z_s (Eq. 13) within a homogeneous halfspace of $\bar{\rho}^{1D}_{a,SSQ} = 19.25\,\Omega\,\mathrm{m}$. Horizontal black dotted lines in Fig. S2 mark the minimum period from which z_p exceeds the average site spacing ($d_{st}/2$, Tab S1) at Aluto (0.7 km) and in the profile arms (5.9 km). For this condition ($z_p > d_{st}/2$), sounding volumes of neighbouring stations overlap.

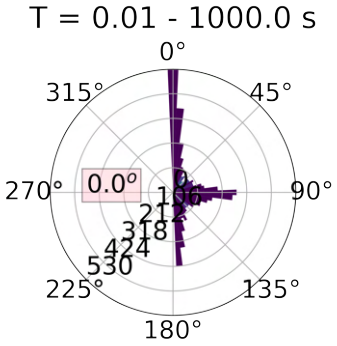

Figure S3: Roseplot histogram in the geographic coordinate system ($N = 0\,^\circ$) of the geoelectric strike ($\alpha - \beta$) inferred from the phase tensor (Eq. 5) for all stations at all frequencies. The given angular direction corresponds to the direction with the maximum number of counts. Ring lines indicate the number of data as given.

Text S3. The MT-dataset of this study clearly demands a 3-D modelling due to 3-D effects observed in the data (Fig. S4). Furthermore, the MT site distribution of our study (see main paper: Fig. 1) requires a multi-scale mesh that would account for the local and the regional site distribution as well as for the varying data resolution.

The mesh we designed for the inversion is shown in Fig. S5. The minimum cell diameters encountered in the mesh are 0.1 km around the site locations at the surface. The cell size increases away from MT stations and with depth to account for the loss of resolution.

Digital Elevation Model given by the NASA SRTM was incorporated into the mesh. This is essential in order to accurately model topography-related galvanic and inductive effects in the data (*Käufl et al.*, 2018).

After topography projection, we assigned a homogeneous resistivity value of $\bar{\rho}^{1D}_{a,SSQ} = 19.25\,\Omega\mathrm{m}$ (Eq. 11) to the subsurface. A data-informed starting model based on the average SSQ impedance (Eq. 10) was shown to be a good choice for data sets with galvanic distortions (*Rung-Arunwan et al.*, 2022).

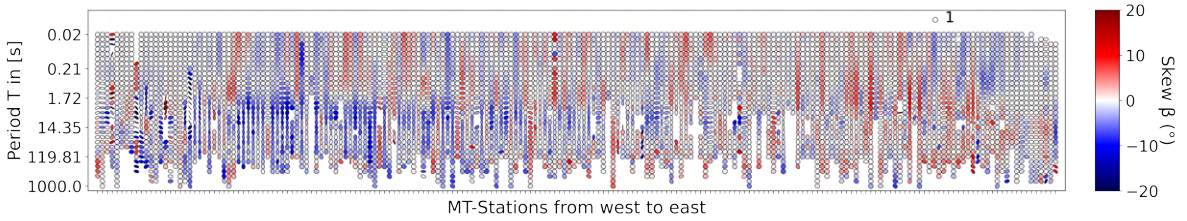

Figure S4: Phase Tensor pseudosection for all stations plotted onto a single line, across the survey area. Phase tensor ellipses were calculated from Eq.5 and are normalized by Φ_{max}. High ellipticities, rapid changes in ellipse main axis directions and high skew values (β) indicate that 3-D effects of the subsurface are present throughout the dataset.

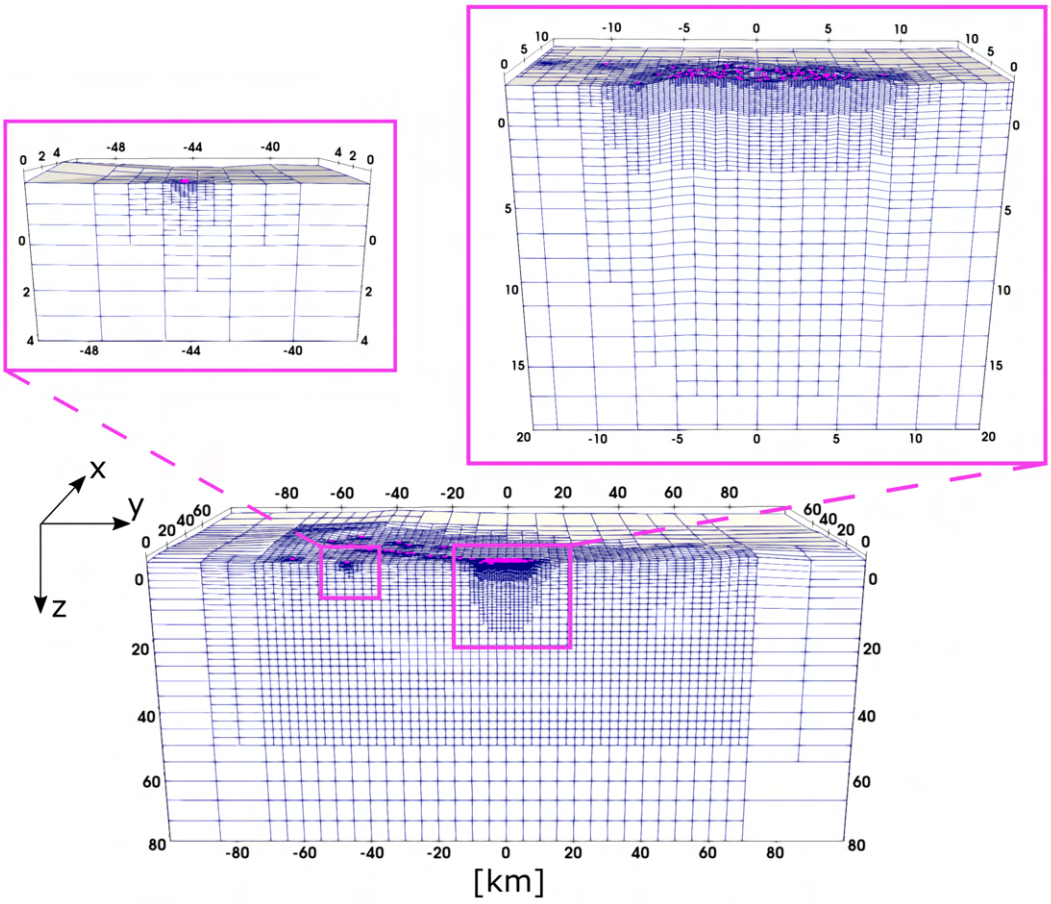

Figure S5: Mesh used in the inversions. The bottom plot shows an EW-slice through the model. The plot on the top left a zoom into a MT site at one of the profile arms, and the plot on the top right a zoom into the mesh at Aluto where a total of 165 MT stations are located. As it is standard in MT the x-axis points to the north, the y-axis to the east and the z-axis is positive downwards.

Text S4. The final model presented in the main paper (Fig. 4) was obtained using a 3-D phase tensor inversion followed by an impedance tensor inversion, whereby the phase tensor model was used as a starting model for the impedance tensor inversion. In the following we present both the phase tensor and impedance tensor models, and provide an in-depth analysis of the data fit for both models.

Text S4.1. Fig. S6 shows the final phase tensor model (corresponding impedance tensor model is shown in Fig. 4 in the main text). We see no major difference between the model in terms of the major large-scale structure. The main features we identified in the impedance tensor model appear equally clear in the phase tensor model: (C1) Aquifer unit, (C2) magma ascent channel, (R1), solidified igneous rock and (C3) lower crustal melt ponding zone.

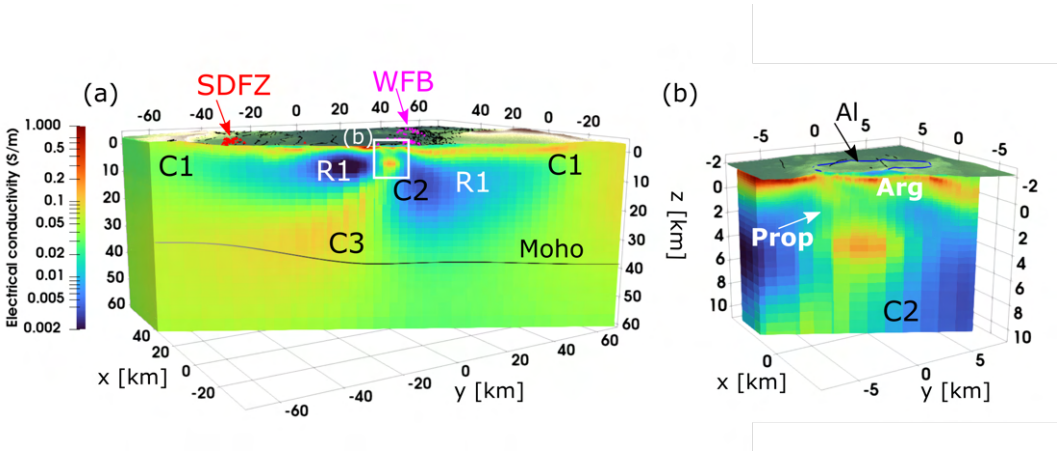

Figure S6: Model obtained from phase tensor inversion. (a) NW-SE oriented profile section, through the obtained model across the entire width of the central MER. The depth of the Moho is taken from (*Stuart et al.*, 2006). Pink and red triangles depict WFB and SDFZ vents respectively. The white box marks the area of the Aluto-Langano geothermal system (b). (b) Close-up of the NW-SE oriented profile section beneath Aluto volcano (Al). Increased conductivities in the shallow subsurface can be attributed to the clay cap formed by argillic alteration (Arg) and higher temperature propyllitic alteration (Prop).

Text S4.2. Pseudosections of the SSQ-averaged apparent resistivities (Fig. S7) and phases (Fig. S8) for the observed and the predicted data of the impedance and the phase tensor model give a qualitative impression of the data fit. Apparent resistivities are generally fitted well by both inversion models, however, absolute values of the impedance tensor model (Fig. S7b) fit the observed data (Fig. S7a) slightly better, compared to apparent resistivity values obtained from the phase tensor model (Fig. S7c). The observed phases are also well fitted by the impedance and the phase tensor model (Fig. S8).

A quantitative measure of the data fit is given by the residuals r and the root-mean-square RMS of observed $\mathrm{F}^{\mathrm{obs}}$ and predicted transfer functions $\mathrm{F}^{\mathrm{pred}}$, where transfer function is either the impedance or phase tensor, depending on the data type that was inverted. The residuals r are defined as follows (see also *Grayver et al.*, 2013):

$$r_i = \frac{\mathrm{F_i^{obs}} - \mathrm{F_i^{pred}}}{\delta \mathrm{F}_i} \quad \text{with} \quad \mathrm{F} \in [\mathrm{Z}, \Phi], \quad i = 1, ..., N, \tag{14}$$

for N data. $\delta\mathrm{F}$ are the propagated data variances of the observed data with an assigned row-wise error-floor of 5% assigned to the impedance tensor as defined in (*Käufl et al.*, 2020). Data

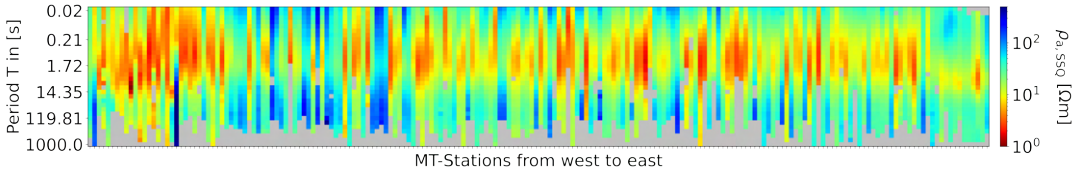

(a) Observed data.

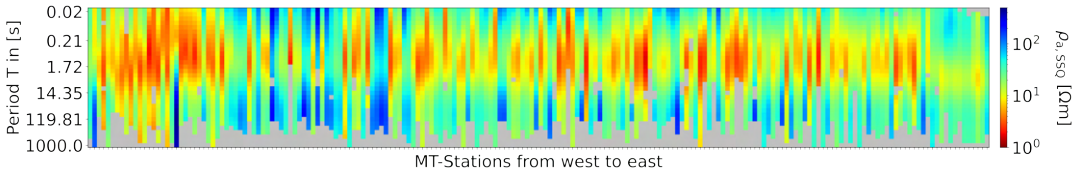

(b) Final model of impedance tensor inversion.

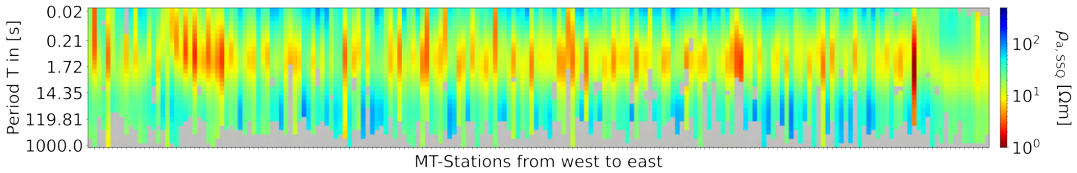

(c) Final model of phase tensor inversion.

Figure S7: Observed and predicted apparent resistivities calculated from $\mathbf{Z}_{SSQ}$ (Eq. 6, Eq. 9) sorted from west to east and projected on the shown "pseudo-profile".

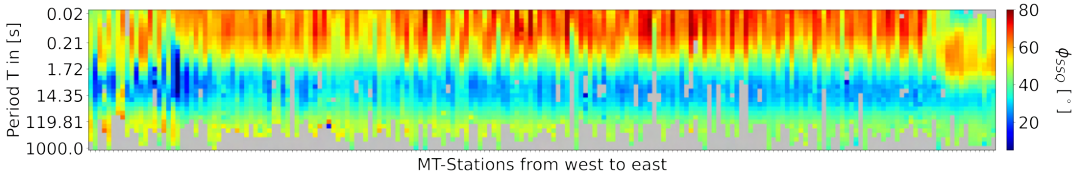

(a) Observed data.

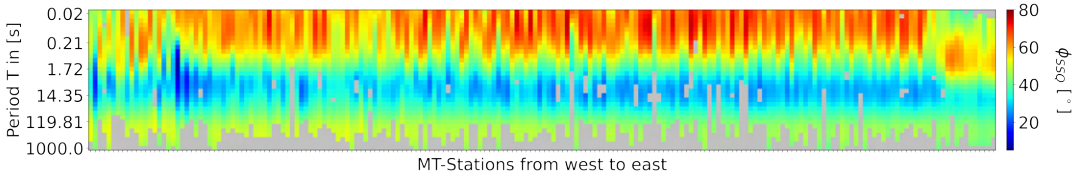

(b) Final model of impedance tensor inversion.

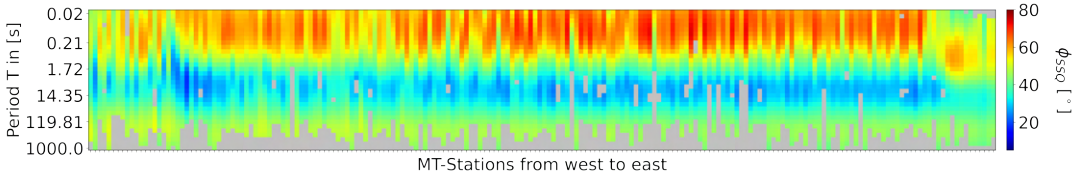

(c) Final model of phase tensor inversion.

Figure S8: Observed and predicted phases calculated from $\mathbf{Z}_{SSQ}$ (Eq. 6, Eq. 9) sorted from west to east and projected on the shown "pseudo-profile".

uncertainties of the phase tensors were obtained by error propagation from the impedance tensor. The RMS is defined as follows:

$$\mathrm{RMS} = \sqrt{\frac{1}{N}\sum_{i=1}^{N} r_i^2} \tag{15}$$

Pseudosections of the RMS-value calculated for all modelled frequencies at all MT-sites are presented for the impedance (Fig. S9a) and the phase tensor (Fig. S9b) models. Both models achieve a good data fit with $(\mathrm{RMS} \leq 1)$ meaning that all data are fitted within the the error bounds at nearly all stations and at all periods.

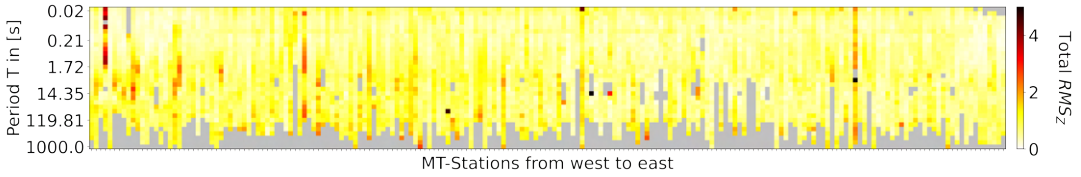

(a) RMS of the impedance tensor model.

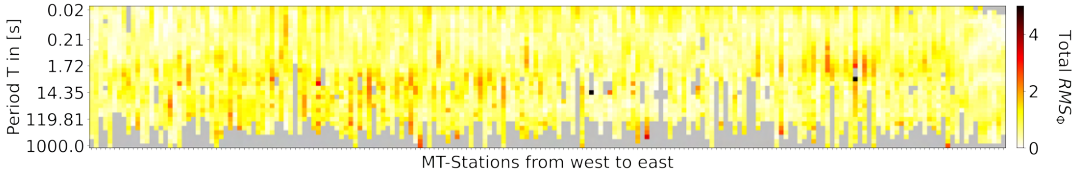

(b) RMS of the phase tensor model.

Figure S9: Achieved RMS of impedance tensor model (a) and phase tensor model (b) presented as pseudosections per MT site and period. Note, that the RMS is always calculated for the respective transfer function used for the inversion (Eq. 14).

Another approach to assess the quality of the fit are crossplots of observed and predicted data (Fig. S10). These crossplots would show a systematic mismatch between observed and predicted data, if a systematic bias exists. Both, apparent resistivities and phase tensor elements, are actually better fitted by the final impedance tensor model (Fig. S10a, Fig. S10b) than by the phase tensor model (Fig. S10c, Fig. S10d). Apparent resistivities calculated from the phase tensor model (Fig. S10c) are less well fitted, reflecting galvanic distortions that are not accounted for in the phase tensor model (see Text S4.3.). It can also be seen that diagonal components of the phase tensor $\Phi_{xx,yy}$ with small magnitudes are generally underestimated (see Fig. S10d).

We conclude that the final impedance tensor model shows an overall good fit of both observed impedance and phase tensors and no systematic mismatch or bias in the data.

Text S4.3. The observed difference in impedance data fit between the final impedance tensor model and the phase tensor model (Fig. S10) is anticipated because: (1) absolute electrical conductivity values are less well constrained in phase tensor inversions compared to impedance tensor inversion (e.g. *Rung-Arunwan et al.*, 2022; *Tietze et al.*, 2015) and (2) the impedance tensors are affected by galvanic distortion, hence the inversion process introduces strong near surface heterogeneities in order to fit distorted responses. This leads to a wider distribution of electrical conductivities recovered by the final impedance tensor model compared to the phase tensor model as illustrated in Fig. S11.

Plane view plots of the surface from both models show that the final impedance tensor model shows a more scattered shallow conductivity structure compared to the phase tensor model (Fig. S12). However, the median of recovered conductivities in both models is identical (Fig. S11). This indicates

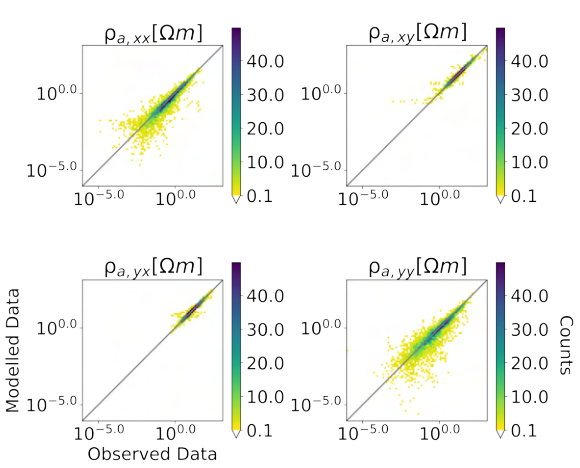

(a) Final model of impedance tensor inversion.

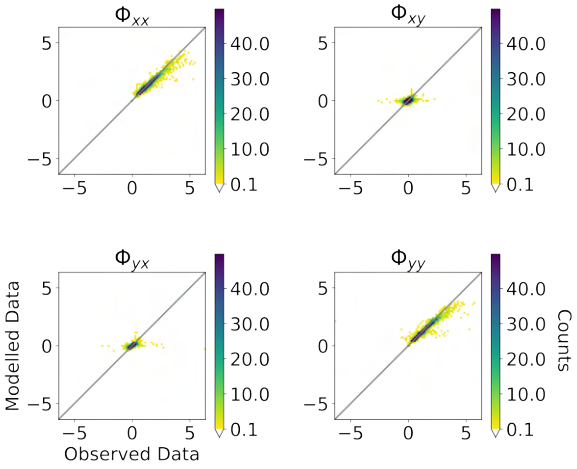

(b) Final model of impedance tensor inversion.

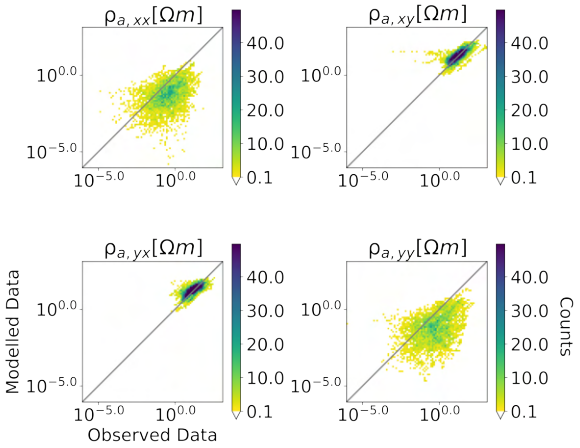

(c) Final model of phase tensor inversion.

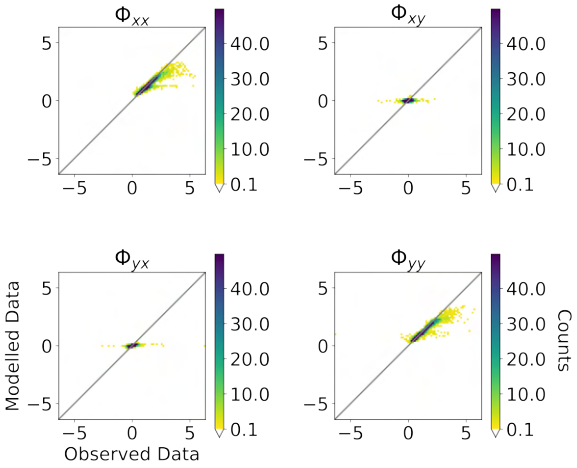

(d) Final model of phase tensor inversion.

Figure S10: Data count crossplots comparing the observed with the predicted apparent resistivity and phase tensors. The gray diagonal line indicates the theoretical distribution for a perfect fit.

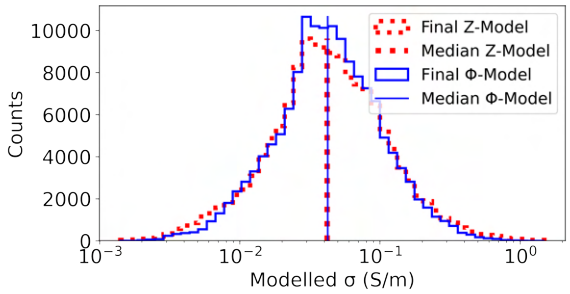

Figure S11: Histogram of predicted conductivities in the final impedance and phase tensor inversion models. Counts refer to the numbers of cells in the mesh with the respective conductivity.

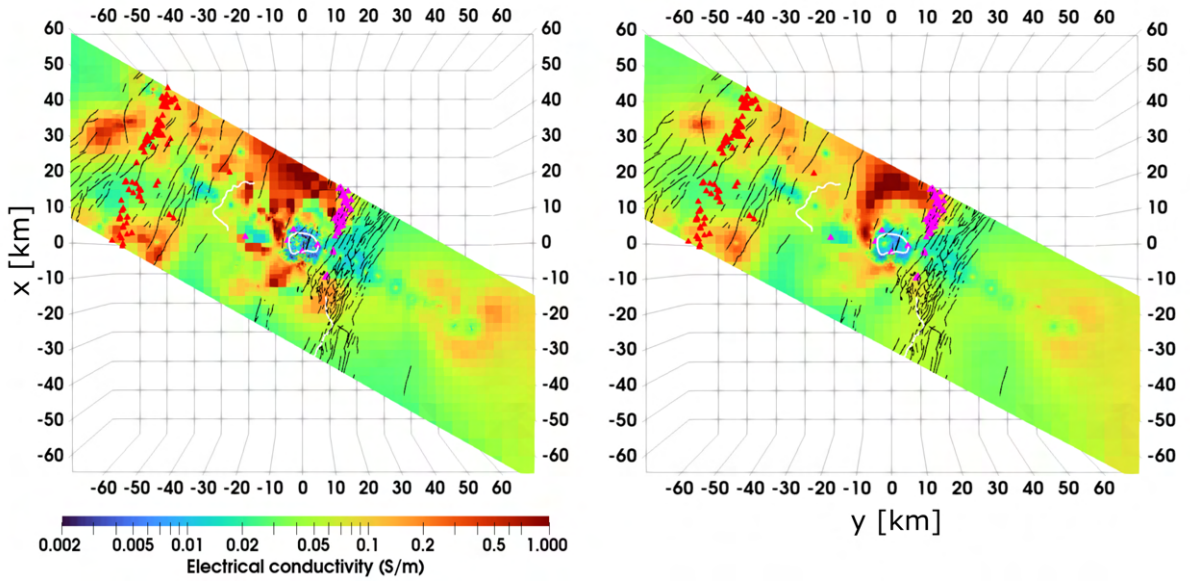

Figure S12: Birdview of the surface from the final model obtained from (a) impedance tensor inversion and from (b) phase tensor inversion. Black lines are fault systems and white lines caldera rims. Triangles are vents in the WFB (magenta) and SDFZ (red).

two important findings: (1) recovered conductivities by the phase tensor inversion are generally in the correct range and (2) impedance tensor inversion only introduces longer tails in the distribution of recovered electrical conductivities, which is due to a need to fit galvanically distorted impedances.

Text S5. The interpretation of recovered electrical conductivities σ_{bulk} in terms of fractions of individual phases present in the considered bulk volume requires knowledge of their electrical conductivities and their degree of connectedness. Magmatic reservoirs and fluid saturated rock are typically described as two-phase systems consisting of a homogeneous rock matrix with conductivity σ_2 and a conducting phase with conductivity σ_1, which is e.g. fluid or magma. For a fully saturated rock, the fraction of the conducting phase χ_1 will be equal to the porosity $\chi_1 = 1 - \chi_2$.

These considerations are summarized in the modified Archies law by (*Glover et al.*, 2000):

$$\sigma_{bulk} = \sigma_1(1-\chi_2)^p + \sigma_2\chi_2^m \quad \text{with} \quad p = \frac{\log(1-\chi_2^m)}{\log(1-\chi_2)}. \tag{16}$$

The degree to which the conducting phase with σ_1 contributes to the bulk electrical conductivity σ_{bulk} depends on its degree of connectedness. A geometrical description of the degrees of connectedness is contained in the cementation component m, which generally increases with the degree of connectedness (*Glover*, 2009). Examples for cementation exponent estimates of end-member geometries are $m = 1$ for a matrix with pores as parallel tubes, $m = 1.5$ for pores in a matrix of closely packed perfect spheres (*Mendelson and Cohen*, 1982; *Sen et al.*, 1981), or $m = 1.15$, which approximates the upper Hashin-Shtrikman bound (*Hashin and Shtrikman*, 1962) and corresponds to the brick-layer model (e.g. *Glover*, 2015).

Text S5.1. In order to relate σ_{bulk} within C3 with basaltic magmatic melt fractions the electrical conductivity of the melt needs to be known under the prevailing conditions. Parameters that predominantly control the electrical conductivity of melt are melt composition, pressure, temperature and the amount of dissolved water within the melt. Estimations of these properties as they are expected to prevail within the lower magmatic ponding zone C3 are summarized in Table S2.

Ni et al. (2011) provides an empirical model that describes the electrical conductivity of basaltic melt for a varying temperature range of $\mathcal{T} = 1200 - 1650\,^\circ\mathrm{C}$ and water content of $c_{H2O}^{melt} = 0.02 - 6.3\,\mathrm{wt}\%$, at a fixed pressure of P=2 GPa (Eq. 17).

$$\log(\sigma) = 2.172 - \frac{860.82 - 204.46\sqrt{c_{H2O}^{melt}}}{\mathcal{T} - 1146.8} \tag{17}$$

$$\text{for} \quad \mathcal{T} = 1200 - 1650\,^\circ\mathrm{C}, \quad c_{H2O}^{melt} = 0.02 - 6.3\,\mathrm{wt}\%, \quad P = 2\,\mathrm{GPa}$$

Note, we extrapolated Eq. 17 to lower pressures of P=1 GPa at $\mathcal{T} > 1300\,^\circ\mathrm{C}$. This is justified according to a study from *Tyburczy and Waff* (1983), who have shown that the influence of pressure on the electrical conductivity can be neglected in this $P-\mathcal{T}$-range. A pressure of 1 GPa is equivalent to an estimated lithostatic depth of 36.6 km (Fig. S13) which corresponds to depths of C3 (see e.g. Fig. S6). In accordance with reported conditions from previous studies (Tab. S2) we estimate melt electrical conductivtiy for a temperatures of $\mathcal{T} = 1300 - 1400\,^\circ\mathrm{C}$ and water contents of $c_{H2O}^{melt} = 0.5 - 1\,\mathrm{wt}\%$. Reported water solubility for parental basaltic melt is $c_{H2O}^{melt} <= 1\,\mathrm{wt}\%$ (*Field et al.*, 2013), which is well in the range of maximum water solubility calculated using MagmaSat ($max: c_{H2O}^{melt} = 6.7\,\mathrm{wt}\%$) (*Ghiorso and Gualda*, 2015) for a quarternary basalt collected from a scoria cone NE of Aluto (sample 17-01-05 from *Gleeson et al.*, 2017). Under these conditions electrical conductivities of basaltic melt will lie within $\sigma_2 = 2.86 - 8.41\,\mathrm{S/m}$ (Fig. S14a).

Using modified Archie's law (Eq. 16) we estimated melt fractions for two different cementation exponents ($m = 1.15, 1.5$) and the minimum and maximum electrical conductivity of basaltic melt $\sigma_2 = 2.86 - 8.41\,\mathrm{S/m}$ (see Fig. S14a). The observed bulk electrical conductivity for the conductor C3 is $\sigma_{bulk} = 0.1 - 0.18\,\mathrm{S/m}$ and the electrical conductivity of the surrounding matrix is assumed to be $\sigma_1 = 0.02\,\mathrm{S/m}$. This results in melt fraction of $1.8 - 7.1\,\mathrm{vol.}\%$ and $4.5 - 14.7\,\mathrm{vol.}\%$ for maximum and minimum basaltic melt conductivities respectively (Fig. S14b).

Property	Value	Method	Region	Study
Temperature [°C]	1125-1200	Basaltic melt composition related to $\mathcal{T}$ and P	MER	*Ayalew et al.* (2016)
	1400-1460	PRIMELT-2: obtain primary melt composition and temperature	MER	*Rooney et al.* (2012)
Pressure [GPa]	1.01-1.24	Basaltic melt composition related to T and P	MER	*Ayalew et al.* (2016)
	1.5-2.5	Back-correct major element compositions of basalt to $\mathrm{Mg\#72}$	MER: Debre Zeyit	*Rooney et al.* (2005)
Water content [wt%]	0.5 at 0.15 GPa	Thermodynamic modelling with MELTS	MER: Aluto	*Gleeson et al.* (2017)
	1.0 at 0.1 GPa	Thermodynamic modelling with MELTS	MER: Boseti, Gedemsa	*Peccerillo et al.* (2003), *Ronga et al.* (2010)
	0.4-1.0 at 430 MPa	$\mathrm{SiO_2}$ Harker diagrams of experimental vs. measured major elements	NMER: Dabahu volcano, Afar	*Field et al.* (2013)
Partial melt [vol.%]	2-7	Numerical modelling for seismic wave velocities	MER uppermost mantle	*Hammond and Kendall* (2016)
	3-5	P-wave velocity equivalent to study by *Mechie et al.* (1994)	MER low mantle	*Mackenzie et al.* (2005)
	2	Relation of shear wave velocity reduction to melt fraction from *Hammond and Humphreys* (2000)	MER low mantle	*Chambers et al.* (2019)
	$\leq$ 0.6	Relation of shear wave velocity reduction to melt fraction from *Hammond and Humphreys* (2000)	MER mantle	*Gallacher et al.* (2016)
	13	MT study, melt estimation using SIGMELTS	Afar region	*Desissa et al.* (2013)
	$\leq$ 7	Back-correlated $\mathrm{FeO*}$ and $\mathrm{SiO_2}$ contents	MER (DZBJ) Parental mantle melt	*Rooney et al.* (2005)

Table S2: Summary of the results from past studies that constrained prevailing conditions for parental magma generation in the MER. Please note that this list is not comprehensive.

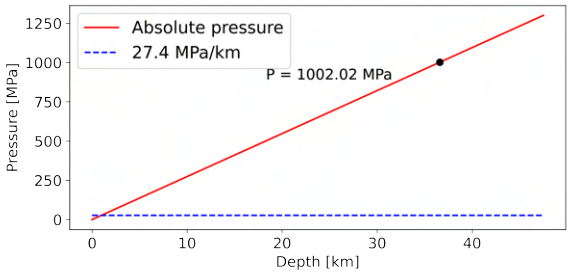

Figure S13: Pressure calculated for a continental crust with $2625\,\mathrm{kg/m^3}$ in a depth of 0-2.5 km and $2800\,\mathrm{kg/m^3}$ for greater depth. These assumptions were reported by *Gleeson et al.* (2017).

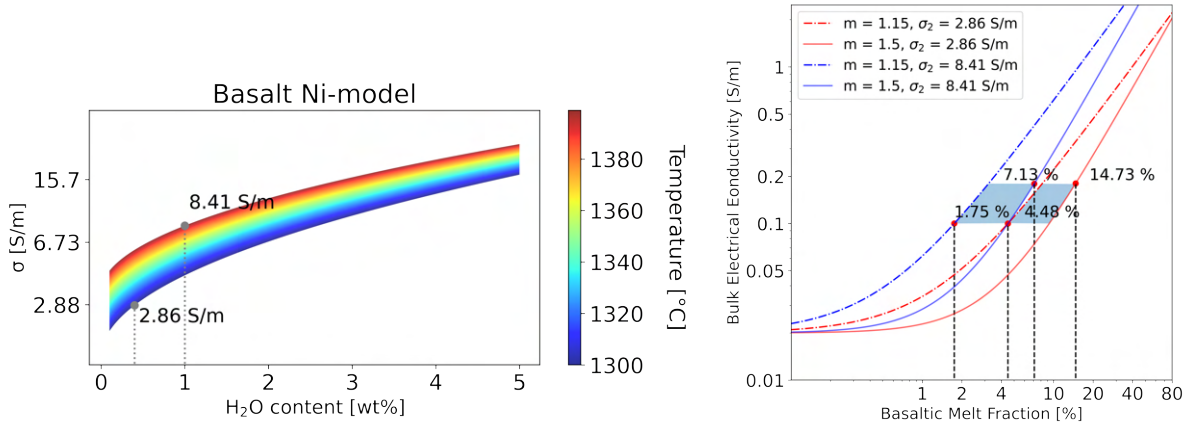

Figure S14: (a) Estimation of σ of basaltic melt after *Ni et al.* (2011) for the given temperature and water content range. (b) Estimation of melt fractions based on the observed bulk electrical conductivities in the lower crustal magma ponding zone using modified Archie's law (Eq. 16). The coloured patches mark the area of observed $\sigma_{bulk} = 0.1 - 0.18\,\mathrm{S/m}$ in the conductor (C3).

Text S5.2. C1 is a prominent electrical conductor that extends at shallow depth over the entire width of the rift (see e.g. Fig. S6). In agreement with the conceptual hydrogeological model of the area by (*Ghiglieri et al.*, 2020) C1 can be interpreted as a fully saturated aquifer system within pyroclastics (ignimbrites) and basalts, where water from the rift shoulders flows into the rift valley.

To verify the interpretation of C1 as an aquifer system with dominating observed bulk conductivities $\sigma_{bulk} = 0.1 - 0.2\,\mathrm{S/m}$ we use modified Archies law (Eq. 16) to estimate the required water fraction within C1. The estimated regional mean electrical conductivity of groundwater is $\sigma_2 = 0.3\,\mathrm{S/m}$ (Fig. S15a).

For the host rock conductivity we assigned $\sigma_1 = 0.05\,\mathrm{S/m}$, which is equivalent to the surrounding rock matrix. The cementation exponent was chosen to be $m = 2.0$, which is in the range of values for sedimentary rocks in upper crustal basins (*Glover et al.*, 2000). Similarly to the estimation of the melt fraction, calculation for estimating the water fraction were perforemd using Eq. 16. Figure S15b shows that a water fraction of $45-79\,\mathrm{vol.\%}$ would be necessary to explain the observed bulk electrical conductivity of $\sigma_{bulk} = 0.1 - 0.2\,\mathrm{S/m}$. However, such high porosities are unrealistic for a compacted pyroclastic rock (Fig. 6 in *Colombier et al.*, 2017; *Sruoga et al.*, 2004).

Hence, the predicted electrical conductivities cannot be solely explained by ionic conduction in fluid-saturated volcanic rock and suggest that the electrical conductivity of the rock matrix is higher than the assumed $\sigma_2 = 0.05\,\mathrm{S/m}$, possibly due to the presence of electrically conductive clays that form through weathering of ignimbrites.

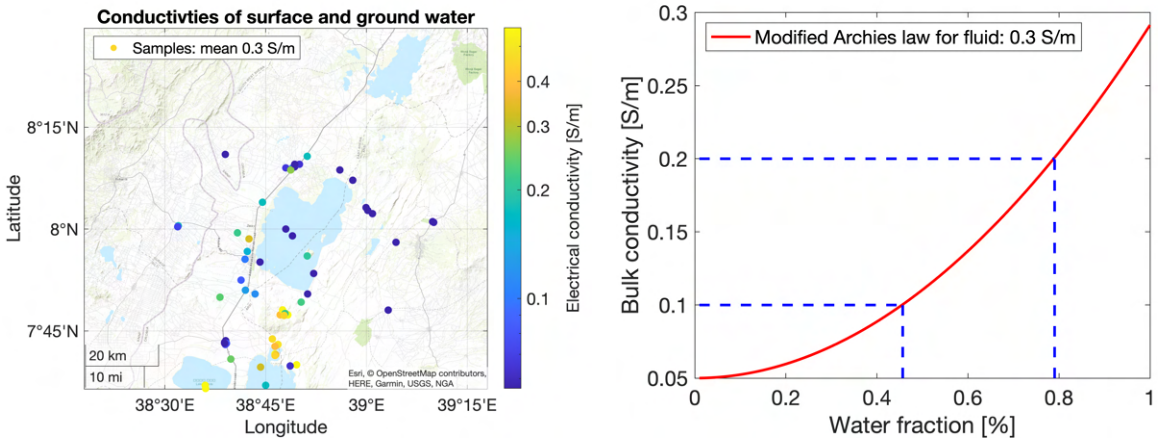

Figure S15: (a) A selection of measured electrical conductivities in the field of surface and groundwaters in the study area, taken from the database of (*Burnside et al.*, 2021). (b) Water fraction present in C1 calculated from the modified Archie's law.

Text S6. To prove that the absence of a high electrical conductivity anomaly beneath the western SDFZ tectono-magmatic segment cannot be attributed to a lack of data sensitivity, we performed a sensitivity test. We placed conductors of different sizes and with a conductivity of $0.1\,\mathrm{S/m}$ in this area (Fig. S16a) and performed forward modelling. The RMS of the forward modelled impedance tensor data increases with respect to the final impedance tensor model, proving that a high conductivity anomaly in this area does not fit the observed data.

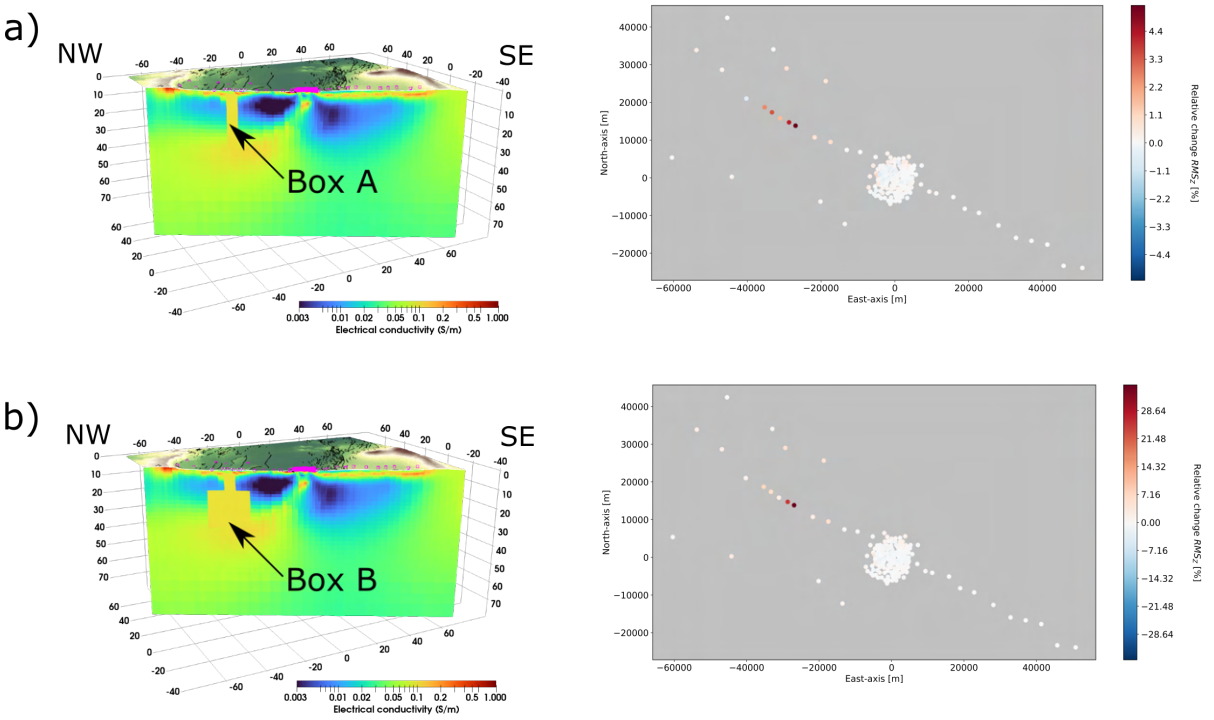

Figure S16: Sensitivity tests investigating the effect of conductivity anomalies placed in the final impedance tensor model beneath the SDFZ as shown in the profile sections. Maps of the relative change in impedance RMS show a maximum increase in misfit at the stations above the synthetic conductivity anomaly. a) Sensitivity test using Box A with 0.1 S/m and a size of $5 * 5 * 29\,\mathrm{km}^3$. b) Sensitivity test using Box B with 0.1 S/m and a size of $9 * 5 * 9\,\mathrm{km}^3$ and $9 * 20 * 20\,\mathrm{km}^3$.

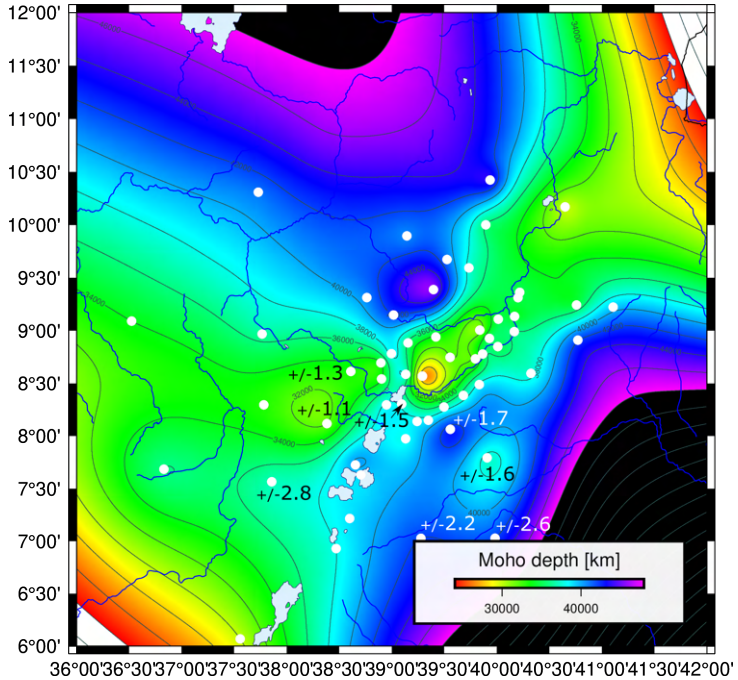

Figure S17: Map of the Moho depth based on data by *Stuart et al.* (2006), numbers under stations (triangles) in the vicinity of the study area are uncertainties on the Moho depth in km as reported by *Stuart et al.* (2006). The map was obtained from laplacian interpolation of the data with minimum curvature using the GMT software.

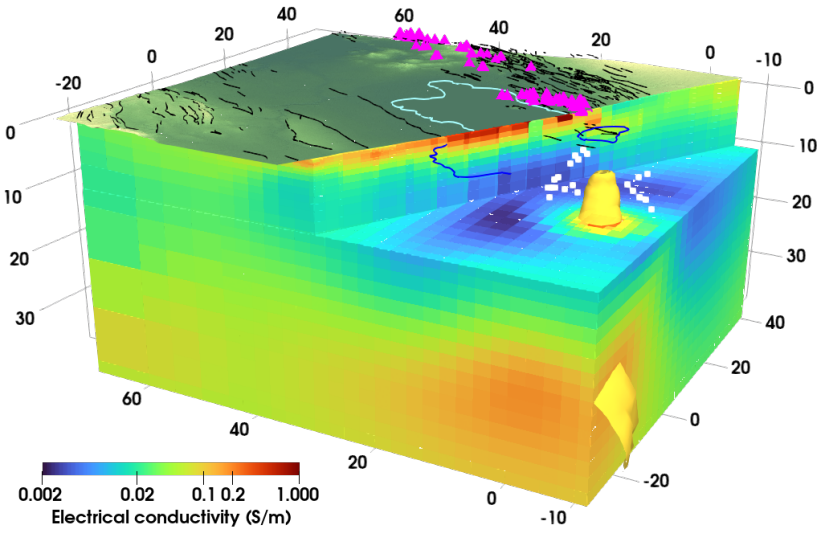

Figure S18: Final impedance tensor model with the 0.1 S/m isosurface depicting the conductivity anomaly C2 interpreted as the magma ascent channel. White squares are seismic hypocenters as reported by *Wilks et al.* (2017).

Movie S1. Animation showing a moving profile slice through the final impedance tensor model along with a 0.1 S/m isosurface, that delineates the lower crustal magma ponding zone (C3) and the magma ascent channel (C2), which terminates beneath Aluto volcano. The animation blends into the conceptual model of the central MER also shown in Fig. 7 of the main paper (video file uploaded separately).

References

Ayalew, D., S. Jung, R. L. Romer, F. Kersten, J. A. Pfänder, and D. Garbe-Schönberg (2016), Petrogenesis and origin of modern Ethiopian Rift basalts: Constraints from isotope and trace element geochemistry, *Lithos*, *258-259*, 1–14, 10.1016/j.lithos.2016.04.001.

Burnside, N., N. Montcoudiol, K. Becker, and E. Lewi (2021), Geothermal energy resources in Ethiopia: Status review and insights from hydrochemistry of surface and groundwaters, *Wiley Interdisciplinary Reviews: Water*, p. e1554, 10.1002/wat2.1554.

Caldwell, T. G., H. M. Bibby, and C. Brown (2004), The magnetotelluric phase tensor, *Geophysical Journal International*, *158*(2), 457–469, 10.1111/j.1365-246X.2004.02281.x.

Chambers, E. L., N. Harmon, D. Keir, and C. A. Rychert (2019), Using ambient noise to image the northern East African Rift, *Geochemistry, Geophysics, Geosystems*, *20*(4), 2091–2109, 10.1029/2018GC008129.

Cherkose, B. A., and H. Mizunaga (2018), Resistivity imaging of Aluto-Langano geothermal field using 3-D magnetotelluric inversion, *Journal of African Earth Sciences*, *139*, 307–318, 10.1016/j.jafrearsci.2017.12.017.

Colombier, M., F. B. Wadsworth, L. Gurioli, B. Scheu, U. Kueppers, A. Di Muro, and D. B. Dingwell (2017), The evolution of pore connectivity in volcanic rocks, *Earth and Planetary Science Letters*, *462*(15), 99–109, 10.1016/j.epsl.2017.01.011.

Desissa, M., N. E. Johnson, K. A. Whaler, S. Hautot, S. Fisseha, and G. J. Dawes (2013), A mantle magma reservoir beneath an incipient mid-ocean ridge in Afar, Ethiopia, *Nature Geoscience*, *6*(10), 861–865, 10.1038/ngeo1925.

Field, L., J. Blundy, A. Calvert, and G. Yirgu (2013), Magmatic history of Dabbahu, a composite volcano in the Afar Rift, Ethiopia, *Bulletin*, *125*(1-2), 128–147, 10.1130/B30560.1.

Gallacher, R. J., D. Keir, N. Harmon, G. Stuart, S. Leroy, J. O. Hammond, et al. (2016), The initiation of segmented buoyancy-driven melting during continental breakup, *Nature Communications*, *7*, 1–9, 10.1038/ncomms13110.

Ghiglieri, G., M. Pistis, B. Abebe, T. Azagegn, T. A. Engidasew, D. Pittalis, et al. (2020), Three-dimensional hydrostratigraphical modelling supporting the evaluation of fluoride enrichment in groundwater: Lakes basin (Central Ethiopia), *Journal of Hydrology: Regional Studies*, *32*, 100,756, 10.1016/j.ejrh.2020.100756.

Ghiorso, M. S., and G. A. Gualda (2015), An H_2O–CO_2 mixed fluid saturation model compatible with rhyolite-MELTS, *Contributions to Mineralogy and Petrology*, *169*(6), 1–30, 10.1007/s00410-015-1141-8.

Gleeson, M. L., M. J. Stock, D. M. Pyle, T. A. Mather, W. Hutchison, G. Yirgu, and J. Wade (2017), Constraining magma storage conditions at a restless volcano in the Main Ethiopian Rift using phase equilibria models, *Journal of Volcanology and Geothermal Research*, *337*, 44–61, 10.1016/j.jvolgeores.2017.02.026.

Glover, P. (2009), What is the cementation exponent? A new interpretation, *The Leading Edge*, *28*(1), 82–85, 10.1190/1.3064150.

Glover, P. (2015), Geophysical properties of the near surface Earth: Electrical properties, in *Treatise on Geophysics*, edited by G. Schubert, 2 ed., chap. 11.04, pp. 89–137, Elsevier Oxford, The address of the publisher, 10.1016/B978-0-444-53802-4.00189-5.

Glover, P., M. Hole, and J. Pous (2000), A modified Archie's law for two conducting phases, *Earth and Planetary Science Letters*, *180*(3-4), 369–383, 10.1016/S0012-821X(00)00168-0.

Grayver, A., K. Tietze, and O. Ritter (2013), RMS-Rather Meaningless Simplification?, in *Proceedings on the 25th Schmucker-Weidelt-Kolloquium für Elektromagnetische Tiefenforschung*, pp. 31–35, Kirchhundem Rahrbach, Germany.

Hammond, J. O., and J. M. Kendall (2016), Constraints on melt distribution from seismology: A case study in Ethiopia, *Environmental Geochemistry and Health, With Special Reference to Developing Countries*, *420*(1), 127–147, 10.1144/SP420.14.

Hammond, W. C., and E. D. Humphreys (2000), Upper mantle seismic wave attenuation: Effects of realistic partial melt distribution, *Journal of Geophysical Research, Solid Earth*, *105*(B5), 10,987–10,999, 10.1029/2000JB900042.

Hashin, Z., and S. Shtrikman (1962), A variational approach to the theory of the elastic behaviour of polycrystals, *Journal of the Mechanics and Physics of Solids*, *10*(4), 343–352, 10.1016/0022-5096(62)90005-4.

Hübert, J., and K. Whaler (2020), Magnetotelluric and transient electromagnetic data from the Main Ethiopian Rift. British Geological Survey. (dataset)., 10.5285/2fb02ed4-5f50-4c14-aeec-27ee13aafc38.

Hübert, J., K. Whaler, and S. Fisseha (2018), The electrical structure of the central Main Ethiopian Rift as imaged by magnetotellurics: Implications for magma storage and pathways, *Journal of Geophysical Research, Solid Earth*, *123*(7), 6019–6032, 10.1029/2017JB015160.

Kalscheuer, T., L. B. Pedersen, and W. Siripunvaraporn (2008), Radiomagnetotelluric two-dimensional forward and inverse modelling accounting for displacement currents, *Geophysical Journal International*, *175*(2), 486–514, 10.1111/j.1365-246X.2008.03902.x.

Käufl, J. S., A. V. Grayver, and A. V. Kuvshinov (2018), Topographic distortions of magnetotelluric transfer functions: A high-resolution 3-D modelling study using real elevation data, *Geophysical Journal International*, *215*(3), 1943–1961, 10.1093/gji/ggy375.

Käufl, J. S., A. V. Grayver, M. J. Comeau, A. V. Kuvshinov, M. Becken, J. Kamm, et al. (2020), Magnetotelluric multiscale 3-D inversion reveals crustal and upper mantle structure beneath the Hangai and Gobi-Altai region in Mongolia, *Geophysical Journal International*, *221*(2), 1002–1028, 10.1093/gji/ggaa039.

Kelbert, A., N. Meqbel, G. D. Egbert, and K. Tandon (2014), ModEM: A modular system for inversion of electromagnetic geophysical data, *Computers & Geosciences*, *66*, 40–53, 10.1016/j.cageo.2014.01.010.

Mackenzie, G. D., H. Thybo, and P. K. Maguire (2005), Crustal velocity structure across the Main Ethiopian Rift: Results from two-dimensional wide-angle seismic modelling, *Geophysical Journal International*, *162*(3), 994–1006, 10.1111/j.1365-246X.2005.02710.x.

Mechie, J., K. Fuchs, and R. Altherr (1994), The relationship between seismic velocity, mineral composition and temperature and pressure in the upper mantle—with an application to the Kenya Rift and its eastern flank, *Tectonophysics*, *236*(1-4), 453–464, 10.1016/0040-1951(94)90189-9.

Mendelson, K. S., and M. H. Cohen (1982), The effect of grain anisotropy on the electrical properties of sedimentary rocks, *Geophysics*, *47*(2), 257–263, 10.1190/1.1441332.

Ni, H., H. Keppler, and H. Behrens (2011), Electrical conductivity of hydrous basaltic melts: Implications for partial melting in the upper mantle, *Contributions to Mineralogy and Petrology*, *162*(3), 637–650, 10.1007/s00410-011-0617-4.

Peccerillo, A., M. R. Barberio, G. Yirgu, D. Ayalew, M. Barbieri, and T. W. Wu (2003), Relationships between mafic and peralkaline silicic magmatism in continental rift settings: A petrological, geochemical and isotopic study of the Gedemsa volcano, Central Ethiopian Rift, *Journal of Petrology*, *44*(11), 2003–2032, 10.1093/petrology/egg068.

Ronga, F., M. Lustrino, A. Marzoli, and L. Melluso (2010), Petrogenesis of a basalt-comendite-pantellerite rock suite: the Boseti Volcanic Complex (Main Ethiopian Rift), *Mineralogy and Petrology*, *98*(1-4), 227–243, 10.1007/s00710-009-0064-3.

Rooney, T. O., T. Furman, G. Yirgu, and D. Ayalew (2005), Structure of the Ethiopian lithosphere: Xenolith evidence in the Main Ethiopian Rift, *Geochimica et Cosmochimica Acta*, *69*(15), 3889–3910, 10.1016/j.gca.2005.03.043.

Rooney, T. O., C. Herzberg, and I. D. Bastow (2012), Elevated mantle temperature beneath East Africa, *Geology*, *40*(1), 27–30, 10.1130/G32382.1.

Rung-Arunwan, T., W. Siripunvaraporn, and H. Utada (2016), On the Berdichevsky average, *Physics of the Earth and Planetary Interiors*, *253*, 1–4, 10.1016/j.pepi.2016.01.006.

Rung-Arunwan, T., W. Siripunvaraporn, and H. Utada (2022), The effect of initial and prior models on phase tensor inversion of distorted magnetotelluric data, *Earth, Planets and Space*, *74*(51), 1–24, 10.1186/s40623-022-01611-8.

Samrock, F., A. Kuvshinov, J. Bakker, A. Jackson, S. Fisseha, staff of Addis Ababa University, and the Geological Survey of Ethiopia (2010), Magnetotelluric and vertical magnetic transfer functions acquired at the Aluto-Langano geothermal field, Ethiopia, 10.17611/DP/EMTF/ETHIOPIA/ETHZ, from the IRIS database, `http://ds.iris.edu/spud/emtf`.

Samrock, F., A. Kuvshinov, J. Bakker, A. Jackson, and S. Fisseha (2015), 3-D analysis and interpretation of magnetotelluric data from the Aluto-Langano geothermal field, Ethiopia, *Geophysical Journal International*, *202*(3), 1923–1948, 10.1093/gji/ggv270.

Samrock, F., A. V. Grayver, B. Cherkose, A. Kuvshinov, and M. O. Saar (2020), Aluto-Langano geothermal field, Ethiopia: Complete image of underlying magmatic-hydrothermal system revealed by revised interpretation of magnetotelluric data, in *Proceedings World Geothermal Congress (WGC 2020+1)*, p. 11054, Reykjavic, Iceland, 10.3929/ethz-b-000409980.

Schmucker, U., and P. Weidelt (1975), Electromagnetic induction in the Earth, *Lecture Notes, Aarhus Univ., Denmark*.

Sen, P., C. Scala, and M. Cohen (1981), A self-similar model for sedimentary rocks with application to the dielectric constant of fused glass beads, *Geophysics*, *46*(5), 781–795, 10.1190/1.1441215.

Sruoga, P., N. Rubinstein, and G. Hinterwimmer (2004), Porosity and permeability in volcanic rocks: a case study on the Serie Tobífera, South Patagonia, Argentina, *Journal of Volcanology and Geothermal Research*, *132*(1), 31–43, 10.1016/S0377-0273(03)00419-0.

Stuart, G., I. Bastow, and C. Ebinger (2006), Crustal structure of the northern main ethiopian rift from receiver function studies, *Geological Society, London, Special Publications*, *259*(1), 253–267, 10.1144/GSL.SP.2006.259.01.20.

Tietze, K., O. Ritter, and G. D. Egbert (2015), 3-D joint inversion of the magnetotelluric phase tensor and vertical magnetic transfer functions, *Geophysical Journal International*, *203*(2), 1128–1148, 10.1093/gji/ggv347.

Tyburczy, J. A., and H. S. Waff (1983), Electrical conductivity of molten basalt and andesite to 25 kilobars pressure: Geophysical significance and implications for charge transport and melt structure, *Journal of Geophysical Research, Solid Earth*, *88*(B3), 2413–2430, 10.1029/JB088iB03p02413.

Weidelt, P. (1972), The inverse problem of geomagnetic induction, *Journal of Geophysics*, *38*, 257–289, 10.1093/gji/35.1.379.

Wilks, M., J.-M. Kendall, A. Nowacki, J. Biggs, J. Wookey, Y. Birhanu, A. Ayele, and T. Bedada (2017), Seismicity associated with magmatism, faulting and hydrothermal circulation at Aluto Volcano, Main Ethiopian Rift, *Journal of Volcanology and Geothermal Research*, *340*, 52–67, 10.1016/j.jvolgeores.2017.04.003.